Supplementary Material

Table S1: Orbital chronological constraints used to construct AICC2023. Sources: A (this work), B (Bazin et al., 2013) and C (Extier et al., 2018).

$\delta^{18}O_{atm}$				$\delta O_2/N_2$				TAC			
EDC depth (m)	Gas age (ka BP)	Uncertainty (years)	Source	EDC depth (m)	Ice age (ka BP)	Uncertainty (years)	Source	EDC depth (m)	Ice age (ka BP)	Uncertainty (years)	Source
1465.61	108.50	1303.84	C	1495.96	117.4	3000	A	645.31	30.95	3000	A
1585.2	120.90	1303.84	C	1652.39	125.8	3000	A	782.86	47.95	3000	A
1706.92	128.80	1303.84	C	1772.83	138.1	3000	A	1337.51	93.85	3000	A
1903.01	160.40	1860.11	C	1823.08	150.1	3000	A	1453.56	107.15	3000	A
1921.37	163.00	1860.11	C	1915.39	164.6	3000	A	1588.23	118.35	3000	A
1931.13	165.20	1860.11	C	1964.71	176	3000	A	1650.52	124.75	3000	A
1997.19	178.30	1860.11	C	2008.15	187.2	3000	A	1747.64	135.95	3000	A
2050.18	191.80	2282.54	C	2065.72	196.8	3000	A	1853.73	150.05	3000	A
2096.02	199.00	2282.54	C	2128.92	210.1	3000	A	1938.82	165.35	3000	A
2139.91	207.90	2282.54	C	2196.61	220.8	3000	A	2121.53	210.05	3000	A
2160.01	209.3	2282.54	A	2232.66	231.7	3000	A	2205.70	222.85	3000	A
2229.99	225.3	1303.84	C	2281.09	240.1	3000	A	2237.52	230.45	3000	A
2232.88	227.60	1253	A	2336.71	253.4	3000	A	2274.72	238.9	3000	A
2258.68	233.2	1486.61	A	2374.24	268	3000	A	2318.83	252.55	3000	A
2300.06	242.20	1140.18	C	2406.67	281.1	3000	A	2383.34	268.95	3000	A
2332.74	248.4	1140.18	A	2438.00	290.4	3000	A	2505.82	313.35	3000	A
2363.62	258.70	1140.18	C	2469.99	302.2	3000	A	2623.99	353.65	3000	A
2376.66	264.40	1140.18	C	2502.46	312.8	3000	A	2633.73	362.125	3000	A
2409.39	279.00	2459.67	C	2536.47	325.1	3000	A	2759.45	417.15	6000	A
2451.16	289.00	2459.67	C	2572.12	334.6	3000	A	2792.11	434.15	6000	A
2466.27	293.90	2459.67	C	2603.71	344.2	3000	A	2815.91	467.05	6000	A
2475.81	301.30	1941.65	C	2622.61	354.1	6000	A	2823.81	475.4	6000	A
2490.37	304.90	1941.65	C	2639.97	366.6	6000	A	2831.30	483.55	3000	A
2522.11	316.60	1303.84	C	2677.69	372.5	6000	A	2850.57	495.45	3000	A
2582.63	334.30	1303.84	C	2685.82	377.8	6000	A	2931.35	556.25	6000	A

2599.92	337.90	1253	C	2763.95	418.1	6000	A	2962.01	569.25	6000	A
2664.62	377.30	1421.27	C	2805.78	454.9	6000	A	2986.85	578.35	6000	A
2679.89	385.70	1627.88	C	2815.83	465.7	6000	A	3000.24	587.95	6000	A
2707.22	398.50	3008.32	C	2820.37	475.4	6000	A	3013.99	599.85	3000	A
2776.91	425.9	1702.94	A	2833.08	484.2	3000	A	3020.93	611.65	3000	A
2784.70	428.8	1702.94	A	2849.73	496	3000	A	3029.38	621.55	3000	A
2791.70	434.5	1702.94	A	2863.56	506.5	3000	A	3035.80	629.75	3000	A
2793.91	440.3	1702.94	A	2880.63	517.3	3000	A	3043.28	642.85	3000	A
2838.23	483.90	4632.49	C	2892.99	525.5	3000	A	3068.47	682.75	10000	A
2857.55	500.60	4632.49	C	2914.24	542.5	3000	A	3078.07	691.55	10000	A
2873.92	504.10	7382.41	C	2929.86	556.2	3000	A	3094.01	703	10000	A
2894.57	521.00	3008.32	A	2951.86	568.4	3000	A	3120.55	715.35	10000	A
2904.64	531.3	3195.31	A	2986.64	577.8	3000	A	3139.92	730.75	10000	A
2909.14	534.90	3195.31	C	3003.49	589.5	3000	A	3148.15	742.55	10000	A
2917.53	549.10	4245	C	3013.24	599.3	3000	A	3160.38	767.45	10000	A
2930.36	555.60	4341.66	C	3021.40	611.3	3000	A	3169.76	779.75	10000	A
2937.72	559.10	3668.79	C	3029.95	620.6	3000	A	3179.04	787.75	10000	A
3002.71	583.00	4632.49	C	3039.12	631.7	6000	A				
3009.86	590.00	4341.66	C	3043.84	644.8	6000	A				
3018.09	602.7	5805.17	C	3052.27	660.7	10000	A				
3017.25	605.08	6000	A	3059.61	671.7	10000	A				
3027.54	615.88	6000	A	3065.69	682.9	10000	A				
3027.9	615.20	8471.72	C	3082.61	691.9	10000	A				
3035.41	622.07	6000	B	3101.62	703.9	10000	A				
3038.00	627.5	6888.4	C	3123.67	714.4	10000	A				
3040.00	633	6888.4	C	3133.92	724.9	10000	A				
3043.01	634.42	6000	B	3141.52	732.5	10000	A				
3043.26	638.2	7481.31	C	3148.60	742.9	10000	A				
3048.51	649.06	6000	B	3155.83	752.1	10000	A				
3056.77	660.79	6000	B	3160.42	758.3	10000	A				
3065.93	676.70	6000	A	3165.19	767.7	10000	A				
3077.74	687.33	6000	A	3172.00	778.8	10000	A				
3093.51	698.16	6000	A	3181.00	787.5	10000	A				

3112.43	708.96	6000	A
3119.57	714.37	6000	B
3124.27	729.38	6000	A
3136.18	733.95	6000	B
3143.2	741.94	6000	B
3152.25	754.18	6000	A
3158.91	763.07	6000	A
3166.87	772.68	6000	A
3174.81	782.61	6000	A
3180.6	797.74	6000	B
3189.83	802.46	6000	A

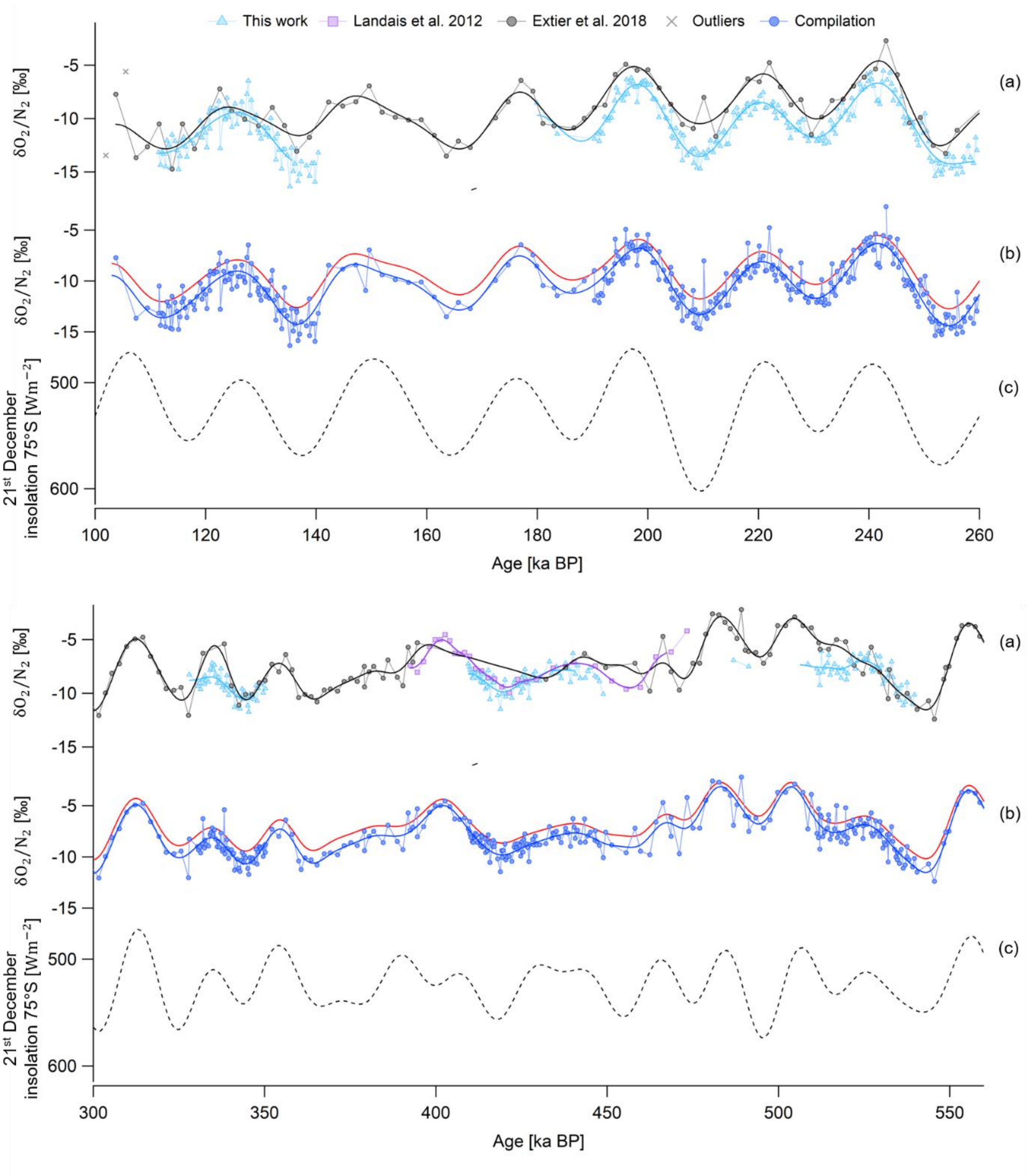

Figure S1. Evolution of EDC $\delta O_2/N_2$ record between 260 and 100 ka BP and between 560 and 300 ka BP. (a) EDC raw $\delta O_2/N_2$ old data between 800 and 100 ka BP (black circles for data of Extier et al. (2018) and purple squares for data of Landais et al. (2012)), outliers (grey crosses) and low-pass filtered signal (black and purple lines). EDC raw $\delta O_2/N_2$ new data (blue triangles, this study) and low-pass filtered signals (blue line). (b) Compilation of the two datasets and low-pass filtered (blue line) or band-pass filtered (red line) compiled signal. (c) 21st December insolation at 75° S on a reversed axis.

Study of the gas loss effect for the EDC $\delta O_2/N_2$ data

The EDC $\delta O_2/N_2$ data have been obtained from several measurement campaigns over the period 2005-2022 at LSCE. We detail in Table S2 the different conditions of storage and measurements of the series.

Table S2: Series of $\delta O_2/N_2$ obtained on the EDC ice cores with details on the storage and conditions of preparation.

Age range (AICC2012, ice age, ka BP)	Date of measurements	Bubbly or clathrate ice	Storage temperature since drilling	Analytical method	Reference
11.3 – 27.06	2006	Bubbly and bubble to clathrate	-20°C	Automated melt extraction line	This study
4.05 – 11.89 & 27.82 – 44.91	2008	Bubbly and bubble to clathrate	-20°C	Automated melt extraction line	This study
100.162 – 116.238	2010	Clathrate	-20°C	Automated melt extraction line	This study
121.19 – 151.32 & 237.7 – 260.27	2007	Clathrate	-20°C	Manual extraction line	This study
157.56 – 208.66	2017	Clathrate	-20°C	Automated melt extraction line	This study
193.14 – 229.19	2022	Clathrate	-20°C	Automated melt extraction line	This study
302.32 – 800	2005	Clathrate	-20°C	Manual extraction line (LSCE)	Landais et al. (2012)
459.77 – 800	2006	Clathrate	-20°C	Manual extraction line (LSCE)	Landais et al. (2012)

392.49 – 473.31	2007	Clathrate	-50°C	Manual extraction line (LSCE)	Landais et al. (2012)
700 – 800	2008	Clathrate	-50°C	Automated melt extraction line (LSCE)	Landais et al. (2012)
103.75 – 136.47 & 338.25 - 700	2012	Clathrate	-50°C	Automated melt extraction line (LSCE)	Bazin et al. (2016)
138.76 – 332.03	2016	Clathrate	-50°C	Automated melt extraction line (LSCE)	Extier et al. (2018)
111.39 – 148.85 & 180.34 – 259.39 & 328.08 – 360.59 & 409.29 – 449.61 & 486.98 – 539.35	2020 - 2022	Clathrate	-50°C	Automated melt extraction line (LSCE)	This study

A correction has been applied on the datasets obtained in 2006 and 2007 because they were obtained on a new mass spectrometer. We found that the calibration of the $\delta O_2/N_2$ data at the time has not be done correctly when switching from the old to the new mass spectrometer and that a shift of +1.5 ‰ should be applied to the $\delta O_2/N_2$ data.

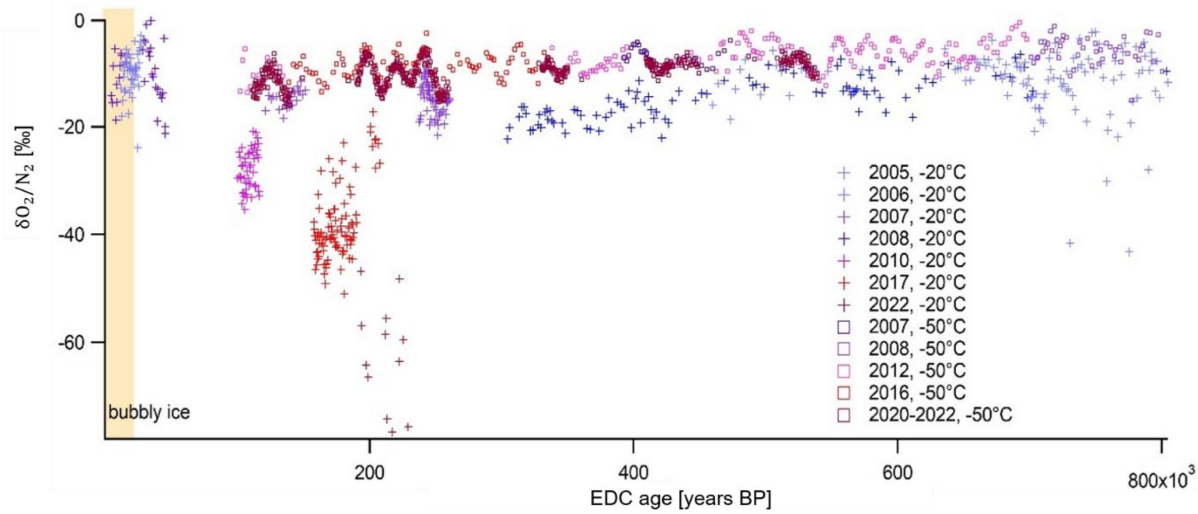

Figure S2: $\delta O_2/N_2$ series from the EDC ice core after different storage conditions. Note that the ice quality was very bad for the ice samples cut at the bottom of the ice core (corresponding to the age range of 800 – 700 ka BP). The yellow rectangle frames the zone with only bubbly ice. The years of measurement are indicated and correspond to the different colors of the series.

Figure S2 shows the evolution of the mean level of $\delta O_2/N_2$ after different storage conditions. We do not notice differences in the $\delta O_2/N_2$ mean level for the samples stored at -50°C even after 14 years of storage (2022 vs 2008). This result is similar to the one obtained at Dome Fuji by Oyabu et al. (2021) even if we are working with smaller sample (20-30 g before removing the outer part). On the contrary, ice storage at -20°C has a strong effect, especially on clathrate ice. The samples analyzed in 2022 after storage at -20°C during more than 18 years exhibit $\delta O_2/N_2$ values as low as -80 ‰. The bubbly ice analyzed here has been stored at -20°C. The associated mean level of $\delta O_2/N_2$ is not significantly different from the one measured for samples stored at -50°C but the scattering is much larger as already observed on other series from bubbly ice (e.g. Oyabu et al., 2021).

Study of the impact of filtering on $\delta O_2/N_2$ – insolation tie point identification

We compare tie point identification performed without (method a) and with (method b) filtering of the highly resolved $\delta O_2/N_2$ record between 260 and 180 ka BP (in Fig. S3). The signal is first interpolated every 100 years. For the method a, we identified the mean maximum (or minimum) position $\mathrm{age}_{\max(i),\mathrm{a}}$ (or $\mathrm{age}_{\min(i),\mathrm{a}}$) as the middle of the age interval $[x_1; x_2]$ in which $\delta O_2/N_2$ is superior (or inferior) to a certain threshold. The threshold is defined as 95% (or 5%) of the amplitude difference D_i between the considered maximum and the minimum immediately preceding it (or between the considered minimum and the maximum immediately following it). The process is reiterated every ~10 kyr (precession half period) when an extremum is reached in the $\delta O_2/N_2$ signal. For the method b (described in the main text), we detected the peak positions ($\mathrm{age}_{\max(i),\mathrm{b}}$ and $\mathrm{age}_{\min(i),\mathrm{b}}$) in the $\delta O_2/N_2$ via an automated method using the zero values of the time derivatives of the low-pass filtered $\delta O_2/N_2$ compiled signal. After comparison of the peak positions identified by methods a and b (Table S3), we found an average disagreement of 700 years, with the largest value, 2150 years, observed between $\mathrm{age}_{\min(i+1),\mathrm{b}}$ and $\mathrm{age}_{\min(i+1),\mathrm{a}}$ at about 230 ka BP (Fig. S3). This period coincides with abrupt variations in the EDC δD record (Fig. S3), reflecting changes in surface climatic conditions which may have impacted high resolution variability of the $\delta O_2/N_2$ signal in addition of the insolation effect. Over periods of lower resolution of the $\delta O_2/N_2$ signal, the extrema positions are not affected by the filtering by more than 600 years (Table S3).

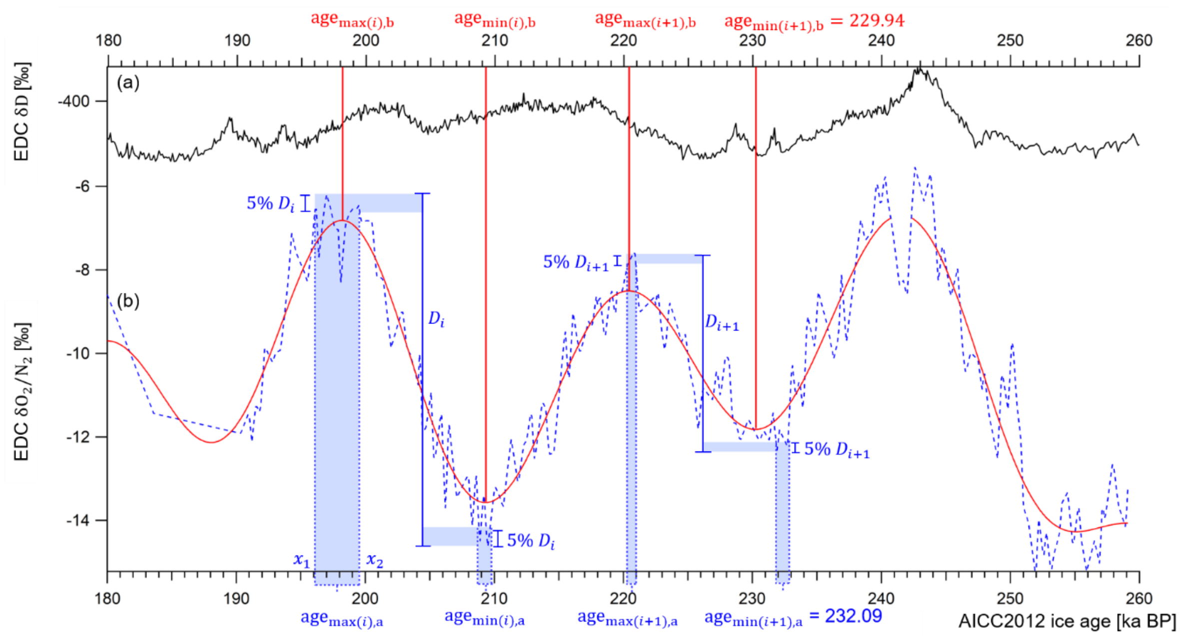

Figure S3. Identification of peaks position in filtered or unfiltered $\delta O_2/N_2$ record between 260 and 180 ka BP. (a) EDC δD (Jouzel et al. 2007). (b) EDC $\delta O_2/N_2$ (blue dashed curve) and low-pass filtered EDC $\delta O_2/N_2$ (red curve). Peaks position in the $\delta O_2/N_2$ record is identified as per methods a or b. Following the method a, the maximum position $\mathrm{age}_{\max(i),\mathrm{a}}$ (on the bottom axis) is the middle of the age interval $[x_1; x_2]$ (blue vertical rectangles) in which $\delta O_2/N_2$ values are superior to 95% of the difference D_i (vertical blue bars). The other peaks position is indicated in a similar way on the bottom axis. Following the method b, the extremum position is given by a 0 value in the time derivative of the filtered $\delta O_2/N_2$ record. The peak positions obtained with the method b ($age_{max(i),b}$, $age_{min(i),b}$) are indicated by red vertical bars and displayed on the top axis.

Table S3: Peak positions of $\delta O_2/N_2$ identified as per method a and method b between 260 and 180 ka BP. The age difference found between methods a and b is calculated. The average age difference is of 700 years and the standard deviation is of 250 years. EDC ice age as per AICC2012 and orbital ages as per Laskar et al. 2004.

Peak position (ka BP)			**Age difference (years)**
Method a	Method b	Insolation	Between methods a and b
197.64	197.94	196.8	300
209.19	209.14	210.1	50
220.69	220.24	220.8	450
232.09	229.94	231.7	2,150
241.84	241.24	240.1	600
			Average: 700 Standard deviation: 250

Sensitivity tests on background lock-in-depth (LID) scenario at EDC site

The background LID scenario can be derived either from the $\delta^{15}N$ data (i.e. experimental LID), or from firn modeling (i.e. modeled LID). We favor the use of $\delta^{15}N$ data when there are available. Over depth intervals where no measurements of $\delta^{15}N$ were made, the LID can be deduced from firn modeling or from a synthetic $\delta^{15}N$ record using the δD - $\delta^{15}N$ relationship (Bazin et al., 2013). In this work, we assess the credibility of three composite LID scenario (Table S4) constructed using the firn model (Bréant et al., 2017) or the synthetic $\delta^{15}N$ record when no data are available. The credibility is defined by the criterion Δ as per:

$$\Delta = \overline{|(\text{analyzed LID } - \text{background LID})|}$$

Δ represents the average absolute value of the mismatch between the background LID (i.e. prior LID provided in input in Paleochrono) and analyzed LID (i.e. the posterior LID given by Paleochrono) scenarios of LID. The weaker is Δ, the closer the background scenario is to the analyzed scenario, meaning that the background scenario is in relatively good agreement with chronological information compelling the inverse model in Paleochrono. On the contrary, the larger is Δ, the more Paleochrono is forced to significantly modify the background scenario which is incompatible with the chronological constraints. Therefore, the larger Δ is, the less credible is the prior LID scenario. It should be noted that the relative error in the prior LID scenario and the age constraints input in Paleochrono are equal in each test, so that the mismatch Δ is only impacted by the value of the prior LID from one test to another. Three background scenarios of LID are tested (Table S4).

Table S4: Three composite background LID scenarios assessed. Test A corresponds to the background LID used to constrain AICC2012 chronology. Test B corresponds to the background LID used in the new AICC2023 chronology. Configuration 1 implies consideration of impurity concentration in the firn model (see Test 1 in the main text, Table 3). Configuration 2 implies **no** consideration of impurity concentration in the firn model (see Test 2 in the main text, Table 3).

	Assessment number			**$\delta^{15}N$ data availability**	**Depth interval (m)**
	A (AICC2012)	B (AICC2023)	C		
LID calculation	From raw $\delta^{15}N$ data assuming a negligible thermal signal.	From $\delta^{15}N$ data corrected for thermal fractionation estimated by the firn model (configuration 1).	From $\delta^{15}N$ data corrected for thermal fractionation estimated by the firn model (configuration 2).	Yes	[345 – 578], [1086 – 1169] and [1386 – bottom]
	From $\delta^{15}N$ synthetic record (using the δD-$\delta^{15}N$ relationship).	From firn modeling (configuration 1) and scaled to experimental LID values.	From firn modeling (configuration 2) and scaled to experimental LID values.	No	[0 – 345], [578 – 1086] and [1169 – 1386]

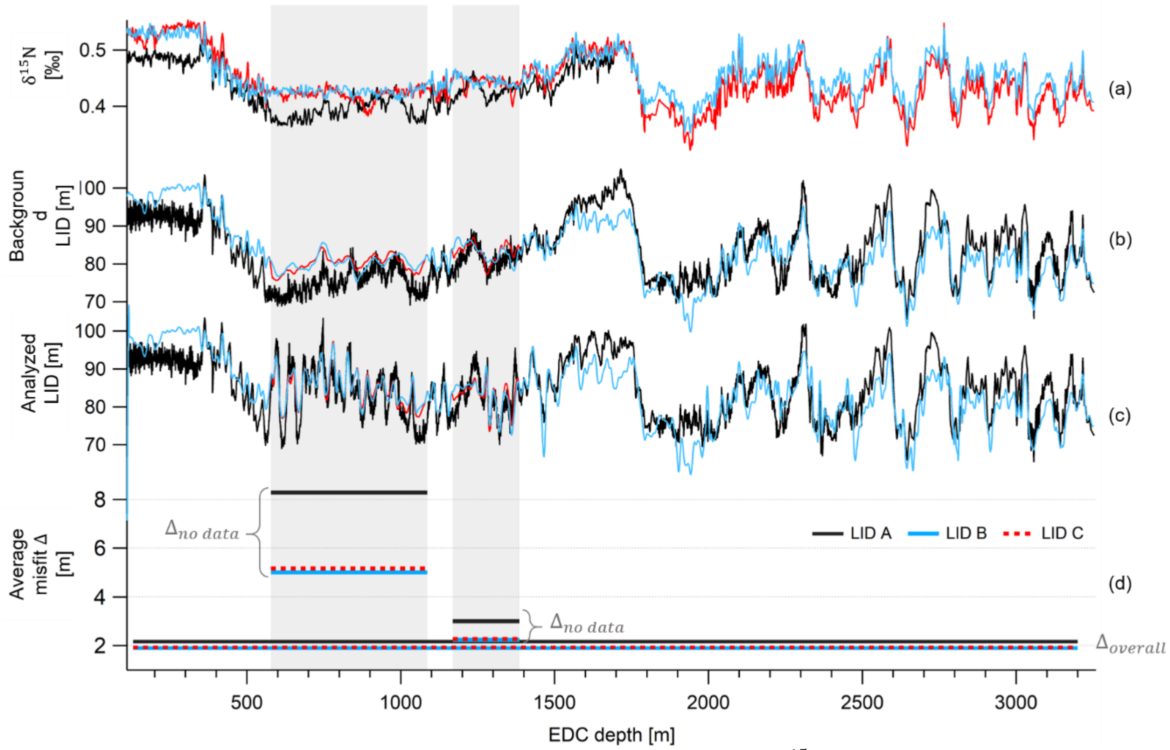

Figure S4. Mismatch Δ between background and analyzed LID for EDC. (a) $\delta^{15}N$ scenario as per tests A (black), B (blue) and C (red). (b) Composite background LID scenario. (c) Analyzed LID scenario. (d) Three averaged values of the misfit Δ are calculated for the three composite LID (black line: LID A, blue lines: LID B, red dots: LID C): $\Delta_{\text{no data}}$, averaged over the two depth intervals where $\delta^{15}N$ data are not available (either between 578 and 1086 m or between 1169 and 1386 m, see intervals shown by grey rectangles), and Δ_{overall}, averaged over the whole 3200 m.

For the construction of the AICC2012 timescale, the background LID scenario at EDC was derived from a synthetic $\delta^{15}N$ record using the δD - $\delta^{15}N$ relationship (Bazin et al., 2013). Yet, this scenario (A, Table S4) is associated with the largest mismatch criterion, $\Delta_{no\ data}$ = 8.3 m, over the last 800 kyr (Fig. S4), hence it is believed to be the least effective among the three tested scenarios and we decided not to use the δD - $\delta^{15}N$ relationship to construct the prior LID scenario in this work.

Modeled LID scenarios (B and C, Table S4) are characterised by smaller mismatch criteria Δ than LID A regardless of the depth interval considered (Fig. S4), hence we believe that firn modeling estimates reproduce well the evolution of past LID at EDC site. In the firn model, the creep factor can be either dependent on impurity inclusion inducing firn softening (giving LID B) or not (giving LID C). The LID sensitivity to the impurity parameter is evaluated by comparing LID B and LID C performances. LID B is associated with the smallest criterion Δ regardless of the depth interval considered (Fig. S4), therefore it is believed to be the most performing and used to constrain the new AICC2023 chronology.

Aligning EDC $\delta^{18}O_{atm}$ record and climatic precession variations

For the construction of the new AICC2023 chronology between 800 and 600 ka BP, the EDC $\delta^{18}O_{atm}$ record has been aligned with the climatic precession delayed or not by 5,000 years depending on the occurrence of Heinrich like events, reflected by peaks in the IRD record from the North Atlantic Ocean. Here, we evaluate the impact on the chronology whether $\delta^{18}O_{atm}$ is aligned with the precession with or without delay. The age shift induced is of 3 kyr on average, reaching its maximum value, of 3.7 kyr, at 712 $\pm$ 2.6 ka BP (red arrow in Fig. S5).

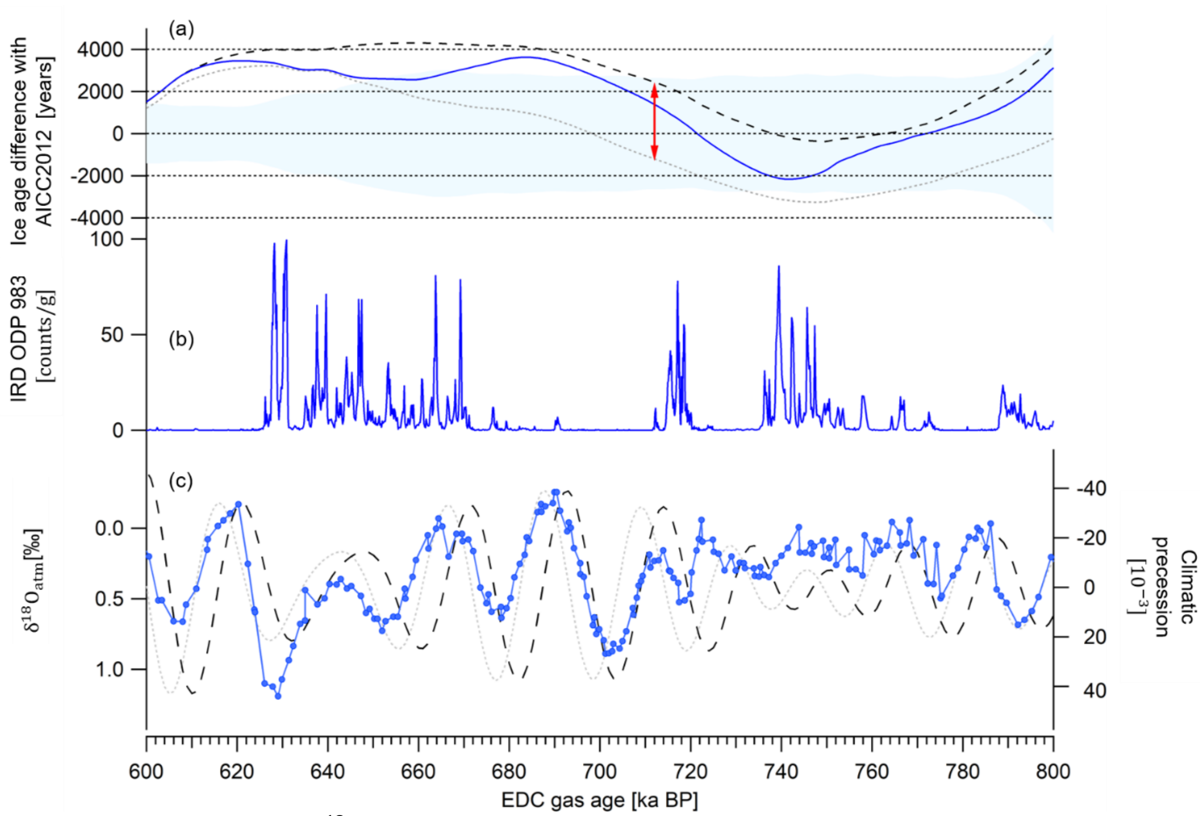

Figure S5. Alignment of EDC $\delta^{18}O_{atm}$ and climatic precession and impact on the chronology between 800 and 600 ka BP. (a) Ice age difference calculated as per (orbital chronology – AICC2012). The orbital chronology is constructed as AICC2023, with different sets of age constraints obtained by aligning $\delta^{18}O_{atm}$ with either 1) 5 kyr delayed precession (grey dotted line), 2) precession (black dashed line) or 3) precession delayed only if Heinrich like events are observed in IRD records (as in AICC2023) (blue line). The largest age difference between chronology 1 and 2 is indicated by the red arrow at 712.0 $\pm$ 2.6 ka BP. (b) Ice-Rafted Debris at ODP983 site (North Atlantic Ocean, southwest of Iceland) by Barker (2021). (c) Compiled EDC $\delta^{18}O_{atm}$ (blue circles). Precession delayed by 5,000 years (grey dotted line) and not delayed (black dashed line) (Laskar et al., 2004).

New background scenarios and dating constraints for Vostok and EPICA Dronning Maud Land (EDML) ice cores

1. Vostok

1.1 New dating constraints

Following the dating approach proposed by Extier et al. (2018), $\delta^{18}O_{atm}$ from Vostok ice core and $\delta^{18}O_{calcite}$ are aligned using mid-slopes of their variations between 370 and 100 ka BP (Fig. S6). To do so, the Vostok $\delta^{18}O_{atm}$ record and the Chinese $\delta^{18}O_{calcite}$ signal are linearly interpolated every 100 years, smoothed (25 points Savitzky-Golay) and extrema in their temporal derivative are aligned. 35 new tie points are identified and attached to an uncertainty between 2.3 and 3.5 kyr. They replace the 35 age constraints obtained by aligning $\delta^{18}O_{atm}$ and delayed precession, associated with a 6 kyr uncertainty and used to construct AICC2012.

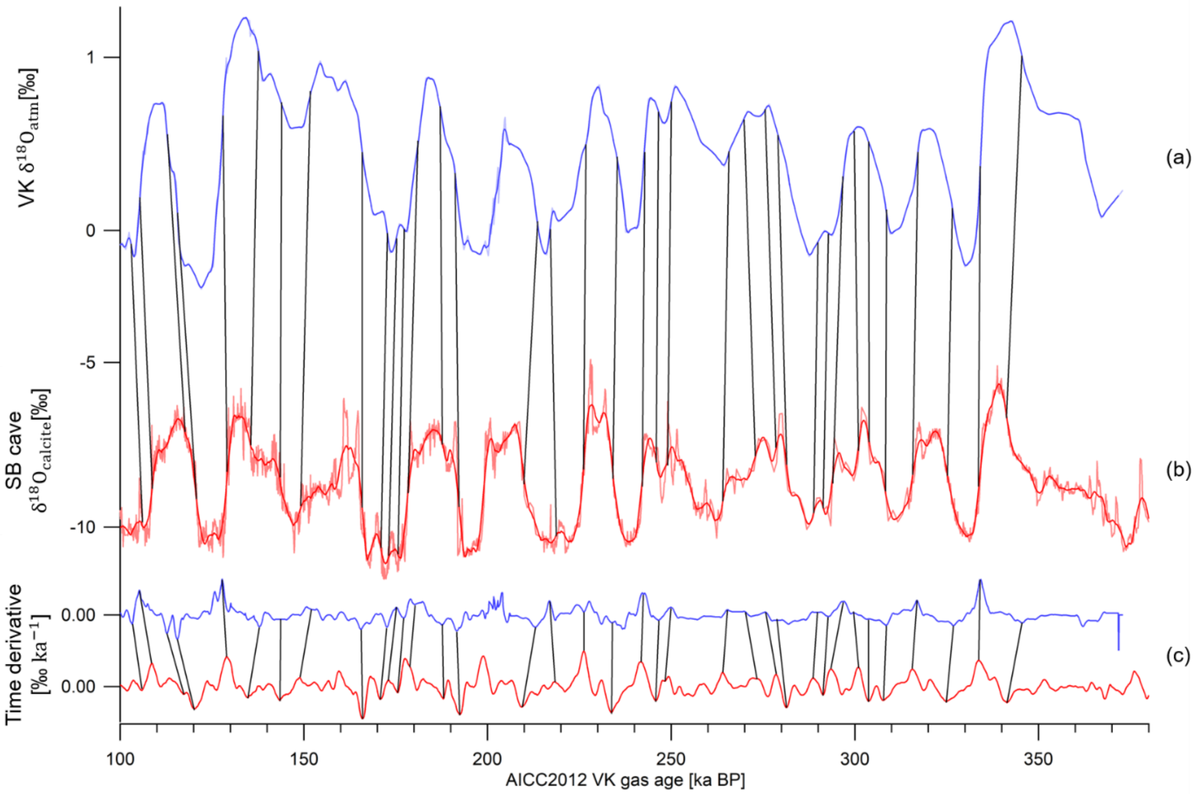

Figure S6. Alignment of Vostok $\delta^{18}O_{atm}$ and Chinese $\delta^{18}O_{calcite}$ records between 370 and 100 ka BP. (a) Vostok (VK) $\delta^{18}O_{atm}$ raw (light blue) and smoothed (dark blue, Savitzky-Golay 25 points) record (Petit et al., 1999). (b) Raw (light red) and smoothed (red) $\delta^{18}O_{calcite}$ from Sambao (SB) cave speleothems. (c) Temporal derivatives of smoothed VK $\delta^{18}O_{atm}$ (blue) and $\delta^{18}O_{calcite}$ (red). Extrema in temporal derivatives are aligned. New tie points are represented by black vertical bars.

1.2 New background LID scenario

When $\delta^{15}N$ measurements are not available, Bazin et al. (2013) used a synthetic $\delta^{15}N$ signal based on the correlation between $\delta^{15}N$ and δD to estimate the background LID scenario at Vostok and to constrain the AICC2012 timescale. In this work, the final background LID scenario is calculated as a function of Vostok depth (Table S5). It is estimated from $\delta^{15}N$ data or $\delta^{40}Ar$ data (which also reflects evolution of the firn thickness) and corrected for thermal fractionation. The thermal fractionation term is estimated by the firn model running in the same configuration as for calculating the modeled LID at EDC (i.e. Test 1, see Table 3 in the main text): firn densification activation energy depending on the temperature and impurity concentration. The final LID scenario has been smoothed using a Savitzky-Golay algorithm (25 points), and then provided as an input file to Paleochrono (Fig. S7).

Table S5. Method of determination of LID background scenario according to Vostok depth range. The thermal fractionation term is estimated by the firn model running in configuration 1 (Table 3): Firn densification activation energy depending on the temperature and impurity concentration.

Depth range (m)	0 – 150	150 – 2737	2737 – 2847	2847 – Bottom
data availability	No	$\delta^{15}N$ (Sowers et al., 1992)	$\delta^{40}Ar$ (Caillon et al., 2003)	$\delta^{15}N$ (Sowers et al., 1992)
LID	From constant $\delta^{15}N$ (measured at 150 m) and corrected for thermal fractionation.	From $\delta^{15}N$ data, corrected for thermal fractionation and smoothed.	From $\delta^{40}Ar$ data, corrected for thermal fractionation and smoothed.	From $\delta^{15}N$ data, corrected for thermal fractionation and smoothed.

2. EDML

When $\delta^{15}N$ measurements are not available, Bazin et al. (2013) used a synthetic $\delta^{15}N$ signal based on the correlation between $\delta^{15}N$ and δD to estimate the background LID scenario at EDML and to constrain the AICC2012 timescale. In this work, the background LID scenario at EDML is estimated from $\delta^{15}N$ data (when available), which is corrected for thermal fractionation. The thermal fractionation term is estimated by the firn model (Test 1, see Table 3 in the main text). Otherwise, the background LID is calculated by firn modeling (Test 1) and its magnitude has been adjusted to the scale of LID values derived from $\delta^{15}N$ data to obtain a coherent scenario. The final LID scenario has been smoothed using a Savitzky-Golay algorithm (25 points), and then provided as an input file to Paleochrono (Fig. S7).

Table S6. Method of determination of LID background scenario according to EDML depth range. The thermal fractionation term is estimated by the firn model running in the same configuration as for calculating the modeled LID, i.e. Test 1 (Table 3): Firn densification activation energy depending on the temperature and impurity concentration. *To obtain a coherent scenario, the modeled LID is adjusted, by standard normalization, to the scale of experimental LID values on the 1398.2 m – bottom depth interval.

Depth range (m)	0 – 548	548 – 1398.2	1398.2 – Bottom
$\delta^{15}N$ data availability	No	Yes (Petit et al. 1999)	No
LID	From constant $\delta^{15}N$ (measured at 548 m) and corrected for thermal fractionation.	From $\delta^{15}N$ data, corrected for thermal fractionation and smoothed.	From firn modeling and scaled* to experimental LID values.

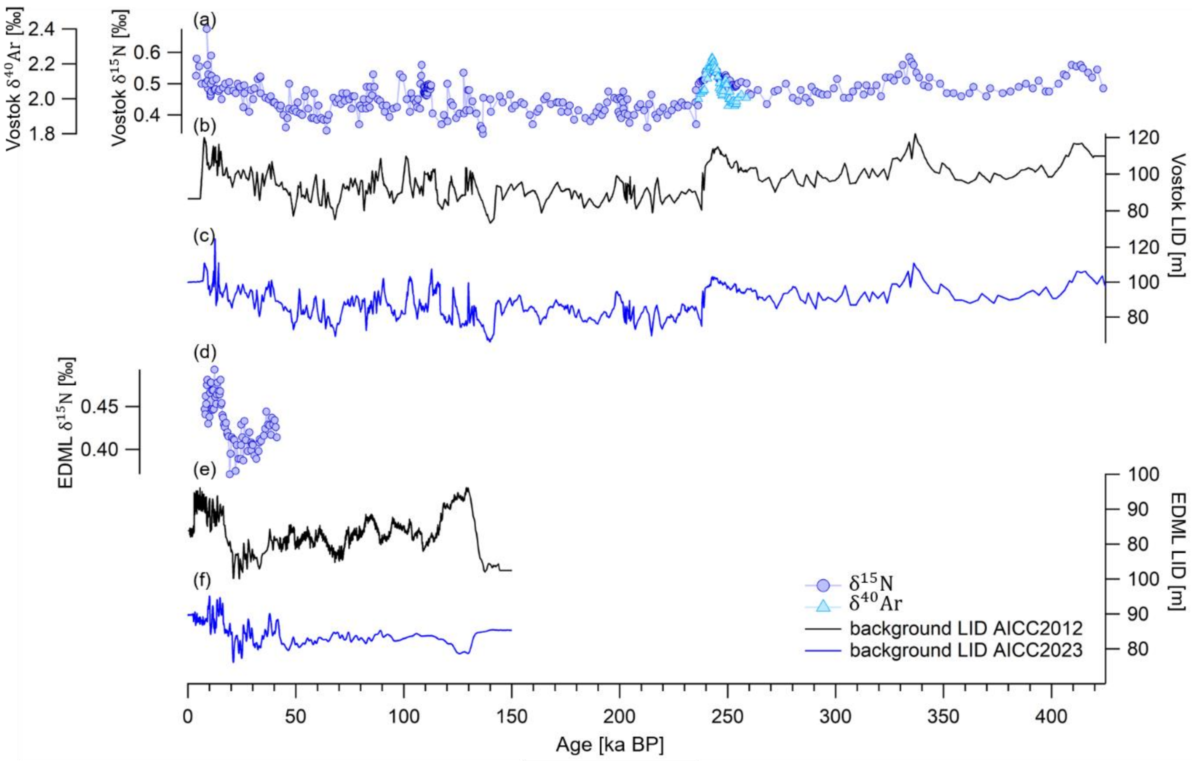

Figure S7. Records of δ^{40}Ar and δ^{15}N and LID scenarios at EDML et Vostok. δ^{15}N and δ^{40}Ar records of Vostok ice core (Sowers et al., 1992; Caillon et al., 2003) (panel a) and δ^{15}N record of EDML ice core (Petit et al., 1999) (panel d). Background LID at Vostok (panel b) and EDML (panel e) used to constrain AICC2012 (Bazin et al. 2013). Background LID at Vostok (panel c) and EDML (panel f) used to constrain AICC2023 (this study).

Such modifications of the background LID scenarios have a negligible impact on the new AICC2023 chronology. Indeed, choosing the scenarios described in this section for EDML and Vostok rather than the scenarios that were used to constrain AICC2012 induces maximum age shifts of 200 and 350 years in the chronology of EDML and Vostok ice cores respectively, which is minor considering the chronological uncertainty of several hundreds of years.

The new AICC2023 chronology for the last 120 kyr

With respect to the AICC2012 chronology, new stratigraphic links between ice and gas series are used to constrain AICC2023 over the past 120 kyr. They include tie points between CH_4 series from EDC, EDML, Vostok, TALDICE and NGRIP ice cores (Baumgartner et al., 2014) as well as volcanic matching points between EDC, EDML and NGRIP ice cores (Svensson et al., 2020) (Fig. S8). To construct AICC2012 over the last glacial period, the Antarctic CH_4 records were synchronized to the NGRIP $\delta^{18}O$(ice) record assuming synchronous variations of global atmospheric CH_4 and North Atlantic temperature during abrupt climatic Dansgaard-Oeschger (D-O) events. Possible inaccuracy of the ice/gas age difference in AICC2012 may have resulted in the offset of several centuries that is observed between Antarctic and Greenland CH_4 records during the rapid increases associated with D-O events (Fig. S8). To fix this offset, we rather use the direct synchronization of CH_4 records to constrain the new AICC2023 chronology. The alignment is improved by several centuries, up to 500 and 840 years for the North Atlantic abrupt warming associated with D-O 5 and 18 respectively.

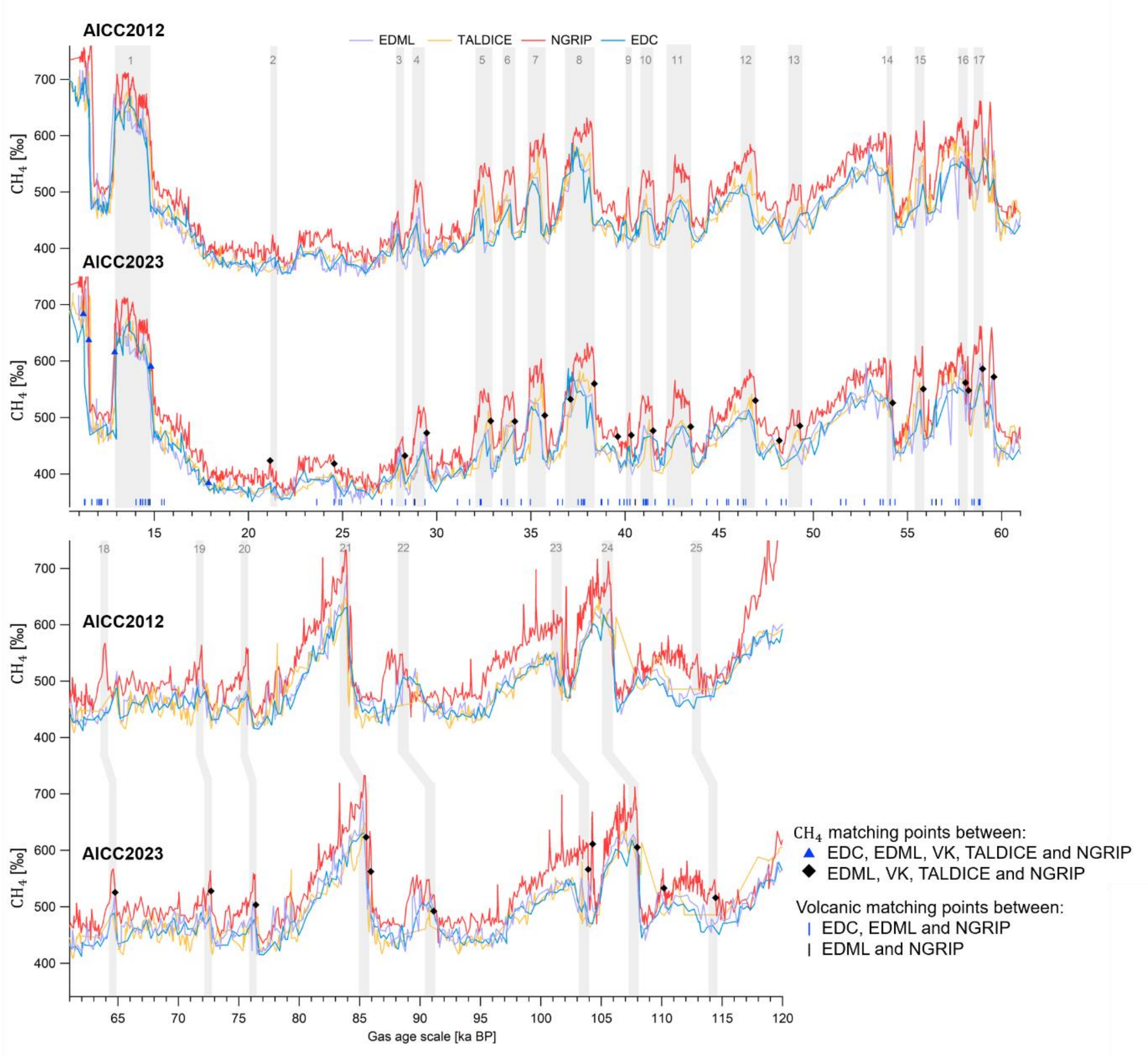

Figure S8. CH_4 records from Antarctic and Greenland sites over the last 120 kyr. CH_4 from EDML, TALDICE, NGRIP and EDC ice cores on the AICC2012 gas timescale (top panel). CH_4 from EDML, TALDICE, NGRIP and EDC ice cores on the AICC2023 gas timescale (bottom panel). Stratigraphic links between CH_4 series from EDC, EDML, Vostok, TALDICE and NGRIP ice cores (blue triangles and black squares, Baumgartner et al., 2014) and between volcanic sulfate patterns from EDC, EDML and NGRIP ice cores (vertical bars, Svensson et al., 2020) are used to constrain AICC2023 over the last 120 kyr. Abrupt D-O events are shown by grey rectangles and numbered from the youngest to the oldest (1-25) (Barbante et al., 2006).

References

Barker, S (2021): Planktic foraminiferal and Ice Rafted Debris (IRD) counts from ODP Site 983: https://doi.pangaea.de/10.1594/PANGAEA.929721, last access: 8 January 2023.

Barbante, C., Barnola, J.-M., Becagli, S., Beer, J., Bigler, M., Boutron, C., Blunier, T., Castellano, E., Cattani, O., Chappellaz, J., Dahl-Jensen, D., Debret, M., Delmonte, B., Dick, D., Falourd, S., Faria, S., Federer, U., Fischer, H., Freitag, J., Frenzel, A., Fritzsche, D., Fundel, F., Gabrielli, P., Gaspari, V., Gersonde, R., Graf, W., Grigoriev, D., Hamann, I., Hansson, M., Hoffmann, G., Hutterli, M. A., Huybrechts, P., Isaksson, E., Johnsen, S., Jouzel, J., Kaczmarska, M., Karlin, T., Kaufmann, P., Kipfstuhl, S., Kohno, M., Lambert, F., Lambrecht, A., Lambrecht, A., Landais, A., Lawer, G., Leuenberger, M., Littot, G., Loulergue, L., Lüthi, D., Maggi, V., Marino, F., Masson-Delmotte, V., Meyer, H., Miller, H., Mulvaney, R., Narcisi, B., Oerlemans, J., Oerter, H., Parrenin, F., Petit, J.-R., Raisbeck, G., Raynaud, D., Röthlisberger, R., Ruth, U., Rybak, O., Severi, M., Schmitt, J., Schwander, J., Siegenthaler, U., Siggaard-Andersen, M.-L., Spahni, R., Steffensen, J. P., Stenni, B., Stocker, T. F., Tison, J.-L., Traversi, R., Udisti, R., Valero-Delgado, F., van den Broeke, M. R., van de Wal, R. S. W., Wagenbach, D., Wegner, A., Weiler, K., Wilhelms, F., Winther, J.-G., Wolff, E., and Members, E. C.: One-to-one coupling of glacial climate variability in Greenland and Antarctica, Nature, 444, 195–198, https://doi.org/10.1038/nature05301, 2006.

Baumgartner, M., Kindler, P., Eicher, O., Floch, G., Schilt, A., Schwander, J., Spahni, R., Capron, E., Chappellaz, J., Leuenberger, M., Fischer, H., and Stocker, T. F.: NGRIP CH4 concentration from 120 to 10 kyr before present and its relation to a δ15N temperature reconstruction from the same ice core, Clim. Past, 10, 903–920, https://doi.org/10.5194/CP-10-903-2014, 2014.

Bazin, L., Landais, A., Lemieux-Dudon, B., Toyé Mahamadou Kele, H., Veres, D., Parrenin, F., Martinerie, P., Ritz, C., Capron, E., Lipenkov, V., Loutre, M.-F., Raynaud, D., Vinther, B., Svensson, A., Rasmussen, S. O., Severi, M., Blunier, T., Leuenberger, M., Fischer, H., Masson-Delmotte, V., Chappellaz, J., and Wolff, E.: An optimized multi-proxy, multi-site Antarctic ice and gas orbital chronology (AICC2012): 120–800 ka, Clim. Past, 9, 1715–1731, https://doi.org/10.5194/cp-9-1715-2013, 2013.

Bazin, L., Landais, A., Capron, E., Masson-Delmotte, V., Ritz, C., Picard, G., Jouzel, J., Dumont, M., Leuenberger, M., and Prié, F.: Phase relationships between orbital forcing and the composition of air trapped in Antarctic ice cores, Clim.. Past, 12, 729–748, https://doi.org/10.5194/cp-12-729-2016, 2016.

Bréant, C., Martinerie, P., Orsi, A., Arnaud, L., and Landais, A.: Modelling firn thickness evolution during the last deglaciation: constraints on sensitivity to temperature and impurities, Clim. Past, 13, 833–853, https://doi.org/10.5194/cp-13-833-2017, 2017.

Caillon, N., Jouzel, J., Severinghaus, J. P., Chappellaz, J., and Blunier, T.: A novel method to study the phase relationship between Antarctic and Greenland climate, Geophys. Res. Lett, 30, https://doi.org/10.1029/2003GL017838, 2003.

Extier, T., Landais, A., Bréant, C., Prié, F., Bazin, L., Dreyfus, G., Roche, D. M., and Leuenberger, M.: On the use of δ18Oatm for ice core dating, Quat. Sci. Rev, 185, 244–257, https://doi.org/10.1016/J.QUASCIREV.2018.02.008, 2018.

Landais, A., Dreyfus, G., Capron, E., Pol, K., Loutre, M. F., Raynaud, D., Lipenkov, V. Y., Arnaud, L., Masson-Delmotte, V., Paillard, D., Jouzel, J., and Leuenberger, M.: Towards orbital dating of the EPICA Dome C ice core using δO 2/N 2, Clim. Past, 8, 191–203, https://doi.org/10.5194/CP-8-191-2012, 2012.

Laskar, J., Robutel, P., Joutel, F., Gastineau, M., Correia, A. C. M., and Levrard, B.: A long-term numerical solution for the insolation quantities of the Earth, Astron. Astrophys, 428, 261–285, https://doi.org/10.1051/0004-6361:20041335, 2004.

Oyabu, I., Kawamura, K., Uchida, T., Fujita, S., Kitamura, K., Hirabayashi, M., Aoki, S., Morimoto, S., Nakazawa, T., Severinghaus, J. P., and Morgan, J. D.: Fractionation of O_2/N_2 and Ar/N_2 in the Antarctic ice sheet during bubble formation and bubble–clathrate hydrate transition from precise gas measurements of the Dome Fuji ice core, Cryosphere, 15, 5529–5555, https://doi.org/10.5194/tc-15-5529-2021, 2021.

Petit, J. R., Jouzel, J., Raynaud, D., Barkov, N. I., Barnola, J. M., Basile, I., Bender, M., Chappellaz, J., Davis, M., Delaygue, G., Delmotte, M., Kotiyakov, V. M., Legrand, M., Lipenkov, V. Y., Lorius, C., Pépin, L., Ritz, C., Saltzman, E., and Stievenard, M.: Climate and atmospheric history of the past 420,000 years from the Vostok ice core, Antarctica, Nature, 399, 429–436, https://doi.org/10.1038/20859, 1999.

Sowers, T., Bender, M., Raynaud, D., and Korotkevich, Y. S.: δ15N of N2 in air trapped in polar ice: A tracer of gas transport in the firn and a possible constraint on ice age-gas age differences, J. Geophys. Res. Atmos., 97, 15683–15697, https://doi.org/10.1029/92JD01297, 1992.

Svensson, A., Dahl-Jensen, D., Steffensen, J. P., Blunier, T., Rasmussen, S. O., Vinther, B. M., Vallelonga, P., Capron, E., Gkinis, V., Cook, E., Kjær, H. A., Muscheler, R., Kipfstuhl, S., Wilhelms, F., Stocker, T. F., Fischer, H., Adolphi, F., Erhardt, T., Sigl, M., Landais, A., Parrenin, F., Buizert, C., McConnell, J. R., Severi, M., Mulvaney, R., and Bigler, M.: Bipolar volcanic synchronization of abrupt climate change in Greenland and Antarctic ice cores during the last glacial period, Clim. Past, 16, 1565–1580, https://doi.org/10.5194/cp-16-1565-2020, 2020.